

# Thermally Assisted Microcutting of Calcium Fluoride Single Crystals



Yan Jin Lee, Akshay Chaudhari, Jiong Zhang and Hao Wang

**Abstract** Optical materials, such as calcium fluoride single crystals, are widely used across various industries for their light transmission capabilities. These materials possess excellent mechanical, physical, and chemical resistant properties but also tend to be very brittle, which poses a challenge to the microcutting of complex freeform shapes with optical surface quality. Ultraprecision single-point diamond turning is commonly used in ductile-regime machining of hard and brittle materials, and polishing is employed as a secondary process to achieve optical quality surfaces, which can be time consuming. To improve the machining efficiency of high-strength materials, hot machining techniques have been developed to improve workpiece plasticity and surface integrity after machining. Surface quality and subsurface damage evaluation of the machined material along with finite element analysis allow a deeper understanding of the effectiveness in heat-assisted machining. In this chapter, an introduction to ultraprecision single-point diamond turning and the fundamentals of ductile-regime machining of hard and brittle materials will be discussed, followed by its application in fabrication of calcium fluoride single crystal lenses. Subsequently, the anisotropic characteristics of calcium fluoride single crystal will be investigated through experimentally validated crack formation models and surface generation morphology to gain detailed appreciation of the challenges faced during production of brittle single-crystal materials. To conclude the chapter, the effects of elevated temperatures on the material properties and machinability will be evaluated using experimental and numerical solutions.

## 1 Optics Fabrication Methods

Different types of materials are employed for various applications depending on the desired material properties such as electrical conductivity, wear resistance, heat con-

---

Y. J. Lee · A. Chaudhari · J. Zhang · H. Wang (✉)  
Department of Mechanical Engineering, Faculty of Engineering,  
National University of Singapore, 9 Engineering Drive 1, Singapore 117575, Singapore  
e-mail: [mpewhao@nus.edu.sg](mailto:mpewhao@nus.edu.sg)

© Springer Nature Singapore Pte Ltd. 2019  
J. Zhang et al. (eds.), *Simulation and Experiments of Material-Oriented Ultra-Precision Machining*, Springer Tracts in Mechanical Engineering,  
[https://doi.org/10.1007/978-981-13-3335-4\\_4](https://doi.org/10.1007/978-981-13-3335-4_4)

ductivity, thermal expansion, light transmissivity, etc. In modern-day industries, there is an increasing demand for precision and accuracy for product development. Excellent surface finish is required for the lenses made of magnesium fluoride ( $\text{MgF}_2$ ) and high-purity fused silica ( $\text{SiO}_2$ ) in the optics industry for efficient light transmission. Lens materials used for lithography often have stringent requirements of refractive index homogeneity and low residual stress-induced birefringence. Calcium fluoride ( $\text{CaF}_2$ ) single crystal is the most economical choice for lithography lens applications with high transmission or low absorption properties less than  $0.002 \text{ cm}^{-1}$  [1, 2].  $\text{CaF}_2$  is also used for infrared and visible wavelength applications such as astronomical instrumentation due to its high transmission from 120 nm to 20  $\mu\text{m}$  [3, 4]. However, the crystal is considered to have a poor machinability due to its brittle nature that can result in structural defects during processing.

The manufacturing of high-quality  $\text{CaF}_2$  encompasses a few stages of processes such as raw material purification, crystal growth through the Czochralski or Bridgman–Stockbarger methods, post-growth annealing, and surface improvement [5–7]. Each stage plays a crucial role in achieving the desired optical properties of the end product. The latter process seeks to reduce surface roughness and remove subsurface damage (SSD) through conventional low-material-removal-rate methods of grinding, lapping, and polishing [8, 9]. However, these machining techniques pose a challenge to fabricate complex-shaped lenses such as an aspherical lens, which has led to the investigation of employing ultraprecision single-point diamond turning (SPDT) as an alternative to achieve complex geometries [10]. Over the last few decades, SPDT has been explored and applied toward the precision machining of brittle materials such as glass, germanium, and silicon [11–13]. These brittle materials commonly fail by fracture with little plastic deformation but can still be deformed plastically on the condition that the stress intensity factor at the machining interface is below the material fracture toughness. This is often determined by the machining parameter “critical depth of cut”, generally associated in the nanometric range of 10–100 nm. Therefore, given no other specially developed technique being employed, the central task in performing ductile-regime cutting of brittle materials like  $\text{CaF}_2$  has been concluded as the determination of the critical depth of cut for a specific work material.

## 2 Machinability of Calcium Fluoride

### 2.1 Slip Model

Like most single crystals, the mechanical properties of  $\text{CaF}_2$  ionic crystal are defined by the formation of cracks through dislocation interactions and anisotropic crystallography behavior [14]. This phenomenon can be explained by the well-known slip line theory that is easily observed in anisotropic materials. Plastic deformation along the slip direction and the cleavage fracture on the cleavage plane are the two fundamental modes of material deformation [11, 15–17]. Mechanical properties such

as hardness and fracture toughness can therefore be determined through the study of slip systems to understand the ductile-mode machining of  $\text{CaF}_2$ . The  $\text{CaF}_2$  single crystal is reported to cleave on the  $\{111\}$  and partially  $\{110\}$  planes, with  $\{100\}$   $\langle 110 \rangle$  primary slip systems and secondary slip systems at  $\{110\}$   $\langle 1-10 \rangle$  [14, 17, 18]. Hardness tests by nanoindentation, Vickers or Knoop microhardness tests are commonly used to assess these mechanical properties. The plastic deformability that is a ratio between Young's modulus and hardness value ( $E/H$ ) can be studied using the Vickers nanoindentation experimental method over varying loads ranging from 20 to 100 mN. The  $E/H$  values of the (100), (110), and (111) planes were calculated to be 70.5, 57.9, and 69.0, respectively, attributing the differences to the indentation orientation with respect to the slip planes [19]. Different crystallographic plane orientations are expected to produce different measures of deformability. According to the slip model, higher plastic deformability should be observed when the applied force direction is parallel to the slip plane.

In micro-Vickers hardness testing, cracks can be observed at the peripherals of the indentations. Testing on the (110) plane has the highest propensity for crack initiation at relatively low loads, which can be explained using the slip model shown in Fig. 2. In this case, the cleavage plane is parallel to the indentation load, and the resultant forces induced by the pyramidal-shaped indenter causes cleavage fracture to occur prior to shearing along the slip planes. Higher loads of 1.0 and 5.0 N were required for crack initiation on the (111) and (100) plane orientations, respectively [20]. The higher plasticity observed when performing indentations on the (100) plane is due to the loading direction being parallel to the slip plane.

Although single crystals commonly exhibit superior mechanical and optical properties, the existence of slip systems in a single crystal results in the anisotropic effect that is a difficult issue to resolve in machining, i.e., directional-dependent material properties. A common observation for anisotropy during machining is the different symmetrical properties when machining on different plane orientations. Multiple works on the (100), (110), and (111) plane orientations have exhibited fourfold, twofold, and threefold symmetries on the machined surface [17, 21–23]. Figure 1 displays a typical outcome of the threefold symmetry on the (111) plane orientation after face machining of  $\text{CaF}_2$ . Each form of symmetry can be observed through a systematic study of the machined surface quality through face machining on each plane orientation and the critical undeformed chip thickness through progressive grooving along different directions of the crystal. These studies on brittle materials are often coupled with force measurements and crack morphology analysis. The detailed experimental design is out of the scope of this chapter and will not be discussed here.

Similarly, indentation tests with the indenter positioned along different crystallographic directions offer another type of anisotropic analysis. The fracture toughness,  $K_c$ , along different crystallographic directions of a single crystal  $\text{CaF}_2$  sample can be determined using the nanoindentation and microhardness indentation techniques [22]. In these tests, the pyramidal-shaped indenter is oriented along different directions and the crack length,  $c$ , is measured for calculation as shown in Fig. 3. The  $K_c$  value can be calculated by Eq. 1 [21, 23]:

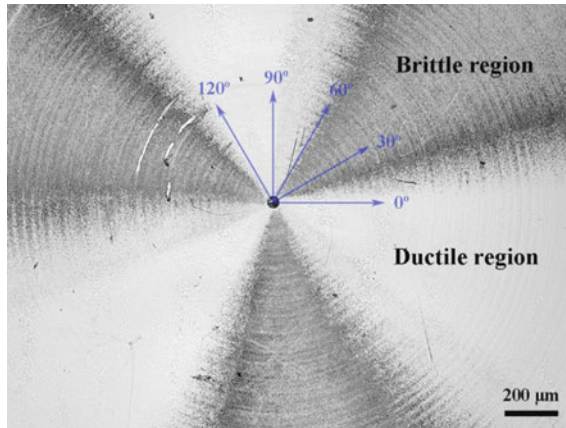


**Fig. 1** Surface morphology of a (111) CaF<sub>2</sub> sample exhibiting the threefold symmetry [22] (reprinted with permission from Springer © 2017)

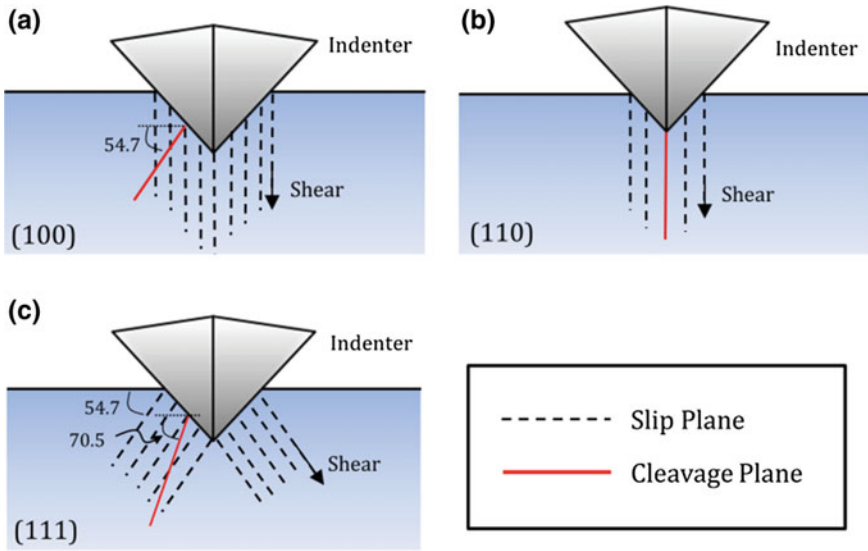


**Fig. 2** Schematic overview of crack initiation mechanism: **a** (100); **b** (110); **c** (111) [24]

$$K_c = (0.016 \pm 0.002) \left( \frac{E}{H} \right)^{\frac{1}{2}} \frac{P}{c^{\frac{3}{2}}} \tag{1}$$

where  $E$  and  $H$  are Young’s modulus and hardness measured from nanoindentation experiments,  $P$  is the applied load in the microhardness test.

The  $K_c$  values were reported to range between 0.325 and 0.675 MPa m<sup>1/2</sup> at room temperature and were in direct correlation with the relative changes in critical

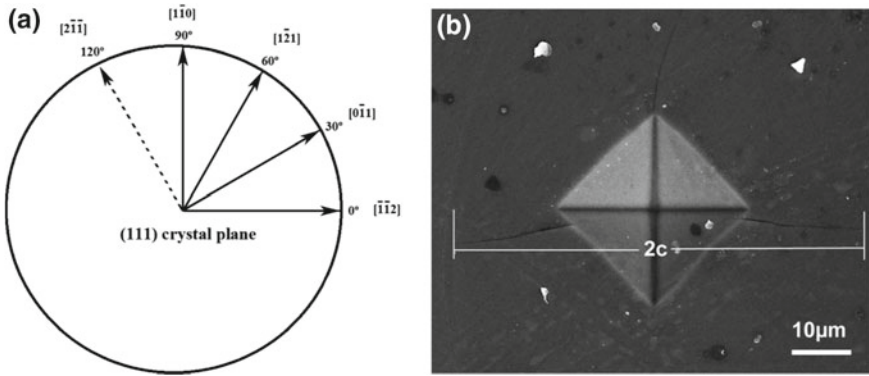


**Fig. 3** **a** schematic of crystallographic directions; **b** SEM image of microhardness indentation and crack formation [22] (reprinted by permission from Springer © 2016)

undeformed chip thickness [22]. It must be noted that different materials exhibit different types of cracking sequence and behaviors [25]. Therefore, this should not be used as a universal method for fracture toughness measurements of brittle materials.

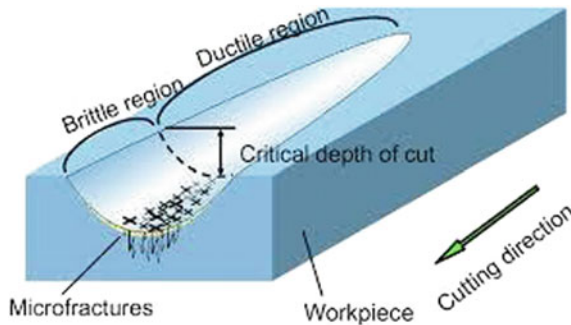
## 2.2 Critical Undeformed Chip Thickness

Optical grade surfaces defined by the fracture-free machined surfaces or mirror-like surfaces have been made possible to machine with technological advances in improving the stiffness and precision controls of conventional machine centers. With the development of ultraprecision machining (UPM) technology, the ductile-regime machining has been realized for hard and brittle materials by accurate control of the cutting process parameters such as the undeformed chip thickness, feed rate, and cutting speed. Of all the tunable process parameters, the undeformed chip thickness is the leading factor that allows ductile-mode machining. Transition to brittle failure occurs when the energy required for plastic deformation exceeds that required for crack initiation [26]. The critical undeformed chip thickness values for machining on different plane orientations of  $\text{CaF}_2$  at room temperature are reflected in Table 1. A range is provided due to the resolved stresses acting along particular crystallographic directions that promote cleavage fractures instead of slipping. In progressive grooving of  $\text{CaF}_2$  along different directions on a defined plane, different types of crack morphologies can be observed. Till date, there has not been any report on the influence of thermal effects on the crack morphologies.

There are a few methods to experimentally determine the undeformed chip thickness values of brittle materials in dynamic machining processes such as plunge cuts. Progressive grooving along the different crystallographic orientations using a diamond cutting tool on the UPM has been the most commonly practiced method

**Table 1** Critical undeformed chip thickness of CaF<sub>2</sub> single crystals of different plane orientations [17]

Plane	Lower limit of undeformed chip thickness (nm)	Upper limit of undeformed chip thickness (nm)	Symmetry characteristic
(100)	140	280	fourfold
(110)	80	300	twofold
(111)	70	380	threefold

**Fig. 4** Schematic of a progressive microgroove [27] (reprinted with permission from Elsevier © 2009)

for quick assessment. The concept of progressive scratching enables a systematic approach to determine the undeformed chip thickness and visually reveals the types of surfaces generated and crack morphologies corresponding to the slip systems of the single crystal. In Fig. 4, two features are commonly observed in a progressive scratch—the ductile region and the brittle region. The ductile–brittle transition depends on the gradient of the scratch. Based on basic geometry, the high gradient will show an immediate change from ductile to brittle and a gradual tilt will show the progressive change in surface generation. Therefore, proper machine tool precision control and selection of grooving parameters should be considered to study the ductile–brittle transition zone.

When considering the influence of the slip theory in ductile-mode machining, cutting speeds are important machining parameters to control to accommodate the speed of dislocation movement in the crystal at room temperature and elevated temperatures. However, cutting speeds are often the limitations of orthogonal grooving experiments due to the mechanical feasibility and do not provide the most accurate representation of the material removal process in an actual cutting process. Excellent machined surface finish on the (111) CaF<sub>2</sub> single crystals with an arithmetic mean height of 1.832 nm can be achieved at maximum cutting speeds of over 35 m/min [21]. However, these speeds are much higher than the allowable one-directional movement speed of 400 mm/min for an average UPM. Alternate UPM setups can be specially constructed such as high-speed shapers that use reciprocating speeds of up to 5.4 Hz and are capable of achieving cutting speeds of 130 m/min [28]. In other

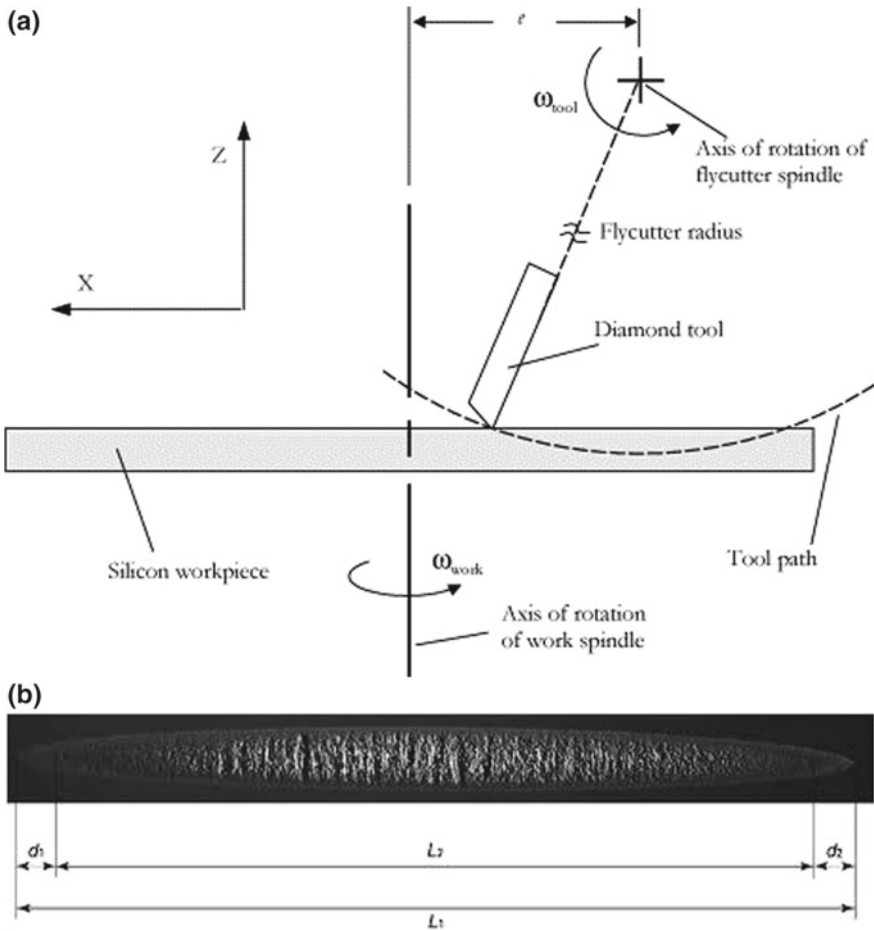


**Fig. 5** Fly cutting approach [29] reprinted with permission from Elsevier © 2017. **a** Cross-sectional schematic of fly cutting scratch on silicon; **b** geometry of scratch made by fly cutting

cases, the fly cutting approach may also be used at realistic cutting speeds to produce similar results to determine the undeformed chip thickness by considering both ends of the groove as shown in Fig. 5.

While indentation tests are commonly used to determine mechanical properties of a material using the slip theory for single crystals, the depth of the indentation is another important result to exploit in determining the critical undeformed chip thickness. Shear stress models resolved along the slip or cleavage planes are commonly used on single crystals when considering the material properties and cutting conditions to describe ductile-regime machining [5, 8, 10].

The first model developed to determine the maximum allowable load,  $P_c$ , during indentation prior to crack initiation using the material fracture toughness,  $K_c$ , and hardness values,  $H$ , is as follows [16]:

$$P_c = \Omega \left( \frac{K_c^4}{H^3} \right) \quad (2)$$

where  $\Omega$  is a normalizing factor that is a function of the ratio of Young's modulus and hardness,  $E/H$ . Blake and Scattergood [30] went on to predict the critical depth of indentation prior to crack indentation as follows:

$$t_c = \psi \left( \frac{E}{H} \right) \left( \frac{K_c}{H} \right)^2 \quad (3)$$

where  $\psi$  is the indenter geometrical constant.

### 2.3 Surface Analysis

There are several commonly used methods to analyze the surface morphology such as white light interferometry (WLI), atomic force microscopy (AFM), scanning electron microscopy (SEM), and Nomarski microscopy. Wang et al. [21] studied the critical undeformed chip thickness along different crystallographic orientations using the contactless WLI measurement as shown in Fig. 6. Surface profiles can be effectively observed along different sections of the groove to determine the roughness and the presence of surface defects through the distortion of the reflected profile.

AFM also offers another highly effective technique for arithmetic mean roughness (Ra) measurement but is normally inferior in terms of measurement area. Yan et al. [10] analyzed the crack-free (111) machined surface of  $\text{CaF}_2$  using the AFM to observe the feed marks and final surface roughness in Fig. 7. They also used the Nomarski microscope to study the critical undeformed chip thickness by reducing the feed rate during end face turning of the sample. Brittle fracture regions can be easily observed at the higher feed rates attributing to the higher undeformed chip thickness values in Fig. 8.

Crack-free surface generation is an important factor in machining optical lenses, but the optimal undeformed chip thickness parameter selected for machining has to be translated to reduced subsurface damage (SSD). The chemical etching method is effective in showing the subsurface dislocation distributions. In fact, a surface prepared by diamond turning reveals more evenly distributed dislocations as compared to a surface produced by polishing. Figure 9 shows the WLI images of etched surfaces that were prepared by different conventional machining methods.

Transmission electron microscopy (TEM) is an excellent equipment for a visual understanding and analysis of subsurface damage induced after machining processes. Lattice rotations, nanocrystal formations, and dislocation activities as a result of the



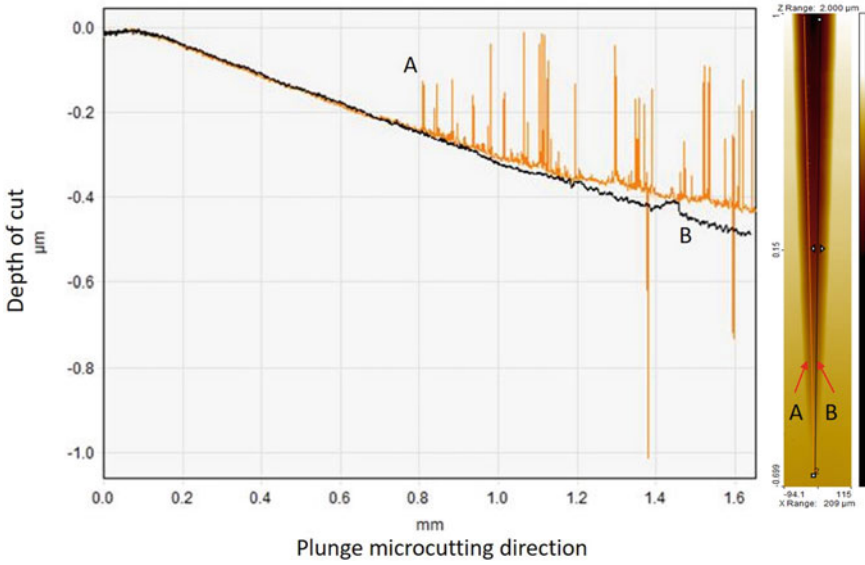


Fig. 6 WLI image of the groove profile made on CaF<sub>2</sub> [21] (recreated with permission from Elsevier © 2016)

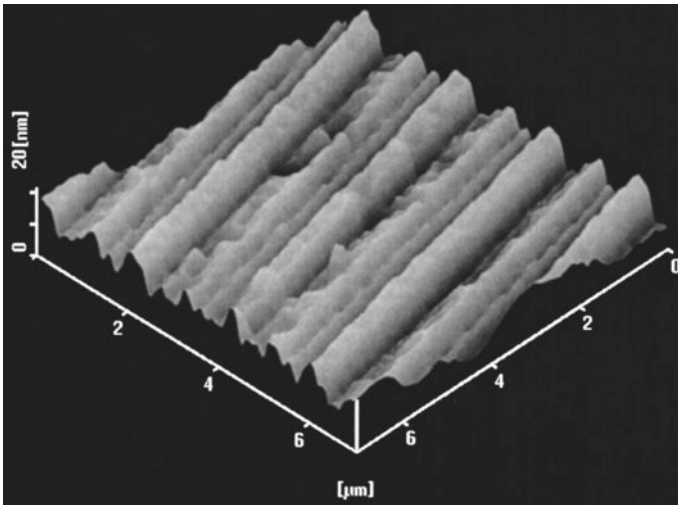
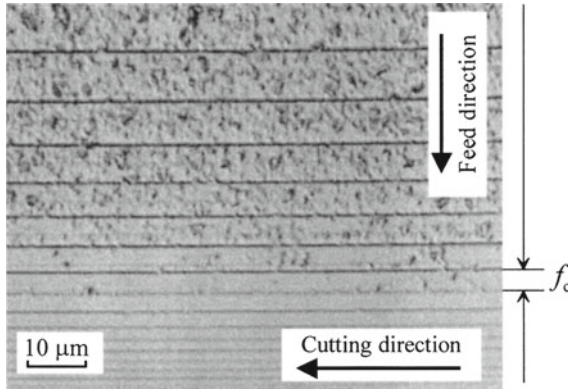
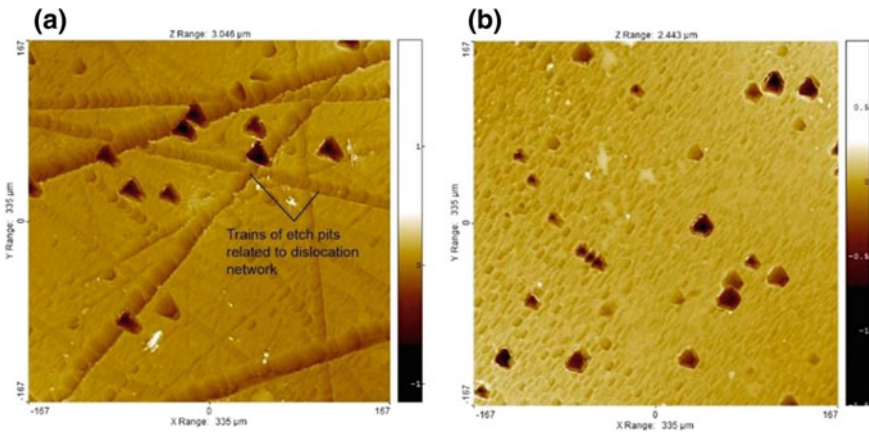


Fig. 7 AFM image of feed lines on the CaF<sub>2</sub> surface with Ra 3.3 nm after machining [31] (recreated with permission from AIP Publishing © 2004)

stresses induced by the machining process can be observed using the high-resolution TEM (HR-TEM) [32]. For effective analysis of the strained lattice structure, TEM samples have to be prepared using a focused ion beam (FIB) system at a crack-free



**Fig. 8** Normarski micrograph of  $\text{CaF}_2$  (111) machined surface at varying feed rates [31] (recreated with permission from AIP Publishing © 2004)



**Fig. 9** Recreated with permission from Elsevier © 2016 **a** concentrated etch pits on optical polished surface; **b** evenly distributed etch pits on diamond turned surface [32]

location on the machined surface as shown in Fig. 10. After which, different locations of the material along the cross-section of the material can be selected to observe the lattice strain and defects using the HR-TEM shown in Fig. 11.

### 2.4 Theoretical Modeling

Various types of theoretical modeling simulations can be used to study the ductile–brittle transition mechanism depending on the scale of simulation. Most macro-sized modeling can be done using the crystal plasticity finite element method

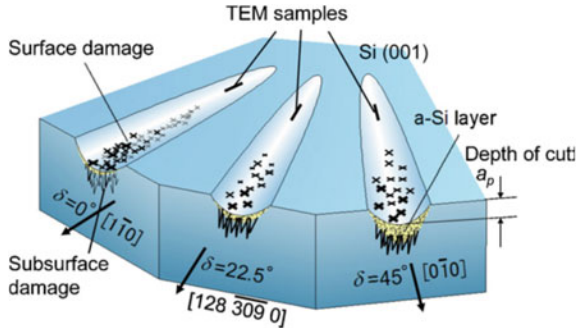


**Fig. 10** Schematic of progressive scratches along different directions and TEM sample extraction locations [33] (recreated with permission from Elsevier © 2012)

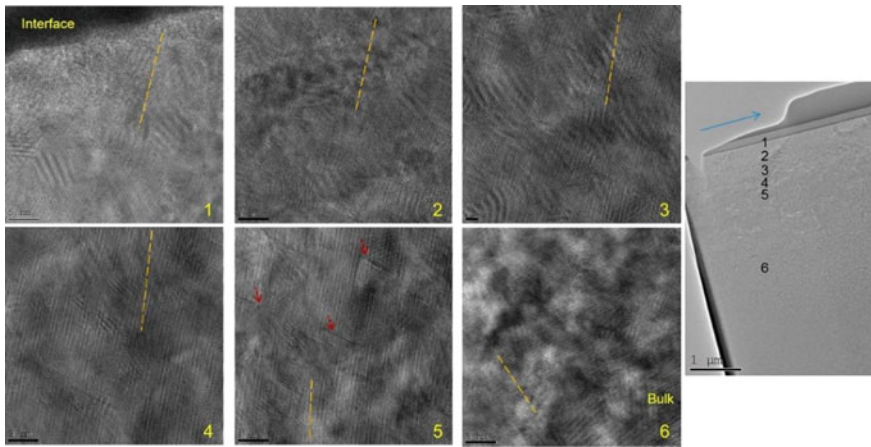


**Fig. 11** HR-TEM images of a machined CaF<sub>2</sub> from the surface (position 1) to the bulk material (position 2). The blue arrow indicates the cutting direction of the groove [32] (recreated with permission from SAGE Publications © 2016)

(CPFEM) and is highly effective when dealing with ductile materials with higher strain rates. Under certain conditions, CPFEM may also be used to study microscale simulations of brittle materials using commercial finite element method (FEM) software ABAQUS/Standard equipped with the UMAT subroutine. Rigid analytical surfaces of the cutting tool are essential to be used in this type of study to reduce computational costs and neglect the influence of tool wear. Crystal plasticity Eqs. 4–7 characterized the crystallographic slip systems governed by Schmid’s law. The slip rate  $\dot{\gamma}^{(\alpha)}$  of slip system ( $\alpha$ ) can first be calculated using the critical resolved shear stress ( $\tau_c^{(\alpha)}$ ), rate sensitive factor ( $m$ ), and strain hardening factor ( $h_{\alpha\beta}$ ) to determine the plastic shear rate ( $\dot{F}^p$ ) as follows:

$$\dot{\gamma}^{(\alpha)} = \dot{\gamma}_0^{(\alpha)} \left| \tau^{(\alpha)} / \tau_c^{(\alpha)} \right|^{1/m} \text{sgn}(\tau^{(\alpha)}) \tag{4}$$

$$\dot{\tau}_c^{(\alpha)} = \sum_{\beta} h_{\alpha\beta} |\dot{\gamma}^{(\beta)}| \quad (5)$$

$$h_{\alpha\beta} = q_{\alpha\beta} \cdot h_0 \left( 1 - \frac{\tau_c^{(\beta)}}{\tau_s} \right)^a \quad (6)$$

$$\dot{F}^P = \sum_{\alpha} \dot{\gamma}^{(\alpha)} s^{(\alpha)} \otimes n^{(\alpha)} F^P \quad (7)$$

where  $s$  and  $n$  are the slip direction and normal to the slip plane, respectively.

This particular method was used to study microcrack formation on the machined surface by calculating the lattice rotation and tensile stresses of selected nodes. By applying the slip model as explained in Sect. 2.1, tensile stresses exceeding a critical value on cleavage plane prior to slip initiation would result in brittle fracture. CPFEM offers effective analysis of stress concentrations of the various deformation zones evolved during a machining process.

CPFEM is also capable of simulating the asymmetric ductile–brittle transition phenomenon seen in orthogonal cutting of  $\text{CaF}_2$  by observing the tensile stresses acting on the tertiary deformation zone. This is done by observing the differences in stress concentrations on both sides of the thin slab that would provide a hint of the nature of the surface generated [21]. This method is preferable as compared to the conventional cubic deformable body method. Cumulative shear strain analysis of each node explains the involvement of slip systems and dislocation activity during an orthogonal cutting process. In general, a higher number of activated slip systems allows ductile material flow that can be observed at the primary plastic deformation zone.

However, CPFEM has its setbacks when modeling the plasticity of brittle materials during UPM due to the microscale time steps in computation. Molecular dynamics (MD) simulations tend to perform more effectively to study atomistic movement and reactions when using various potentials for calculations. Xiao et al. [34] describe in detail the various types of potentials applied and their limitations toward the study of the ductile–brittle phenomenon. It was explained that the Tersoff potential is not suitable in the modeling of brittle materials due to it being a short-ranged bond order potential that often predicts ductile failure rather than to accurately present brittle fracture. On the other hand, the Stillinger–Weber potential and modifications are capable of predicting the brittle failure accurately.

MD simulations offer analysis of the point of crack initiation, direction of crack propagation, and stress distribution around the machining interface. When modeling the orthogonal cutting of 6H SiC, Xiao et al. [34] observed the crack initiation and directionality at sufficiently high undeformed chip thickness settings and discovered that crack formation ahead of the cutting tool is the main cause of crater formation on machined surfaces. This spectacle can be seen in Fig. 12 where the nature of crack initiation and the direction of the crack propagation are dependent on the crystallographic orientations of the machined workpiece.

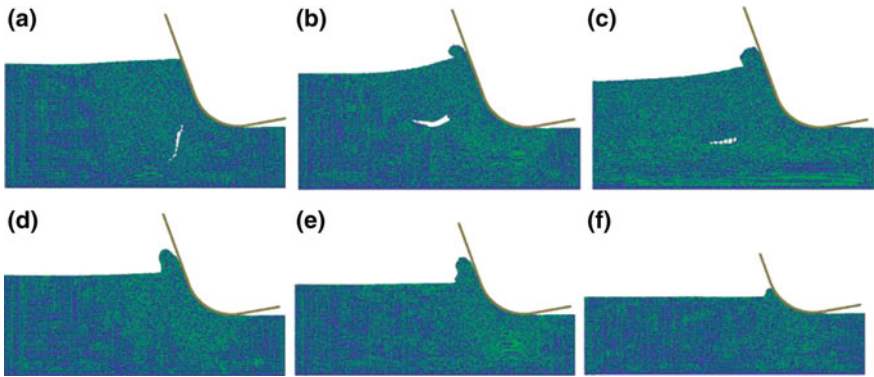


**Fig. 12** MD simulation of orthogonal cutting of 6H SiC at varying undeformed chip thickness parameters [34] (recreated with permission from Elsevier © 2015)

### 3 Analysis of Thermal Assistance

#### 3.1 Thermal Effects on Material Properties

In Sect. 2.1, slip model, it was explained that indentation tests were capable of verifying the mechanical properties and relating the influence of the slip and cleavage planes to crack initiation. Generally, hardness and modulus values tend to decrease with increase in temperature for both ductile and brittle materials [33, 34]. Similarly, experimental work of indentations at the elevated temperatures provides insights into the influence of the additional heat on the crack initiation mechanisms. Vickers microhardness tests conducted at elevated temperatures show decreased material hardness and an increase in indentation depths prior to crack initiation.

Deadmore and Sliney [35] applied a 0.5 N load at a constant indentation rate and dwell time to  $\text{CaF}_2$  and  $\text{BaF}_2$  single crystals over a range of temperatures from 25 to 670 °C. They observed a 40% decrease in hardness at 100 °C and the absence of indentation crack formation at temperatures above 85 °C. Another study on thermally assisted microhardness indentation studies on  $\text{CaF}_2$  single crystals of different plane orientations (100), (110), and (111) with a load of 0.5 N showed a conversion of hardness values at 100 °C in Fig. 13. Thermally assisted indentation shows the potential in reducing the anisotropic effects that can be highly beneficial in an evenly distributed residual stresses and subsurface damage on the machined surface.

The material hardness dropped remarkably by approximately 50% at 100 °C in this test. Differences in results by different authors could be attributed to the different indentation orientations that have an effect on the resolved stresses relative to the slip and cleavage planes as discussed in Sect. 2.1. As expected, elevated temperatures promote slip activation prior to cleavage fracture and increase the indentation depth required for crack formation. Figure 14 shows the improvement in crack initiation

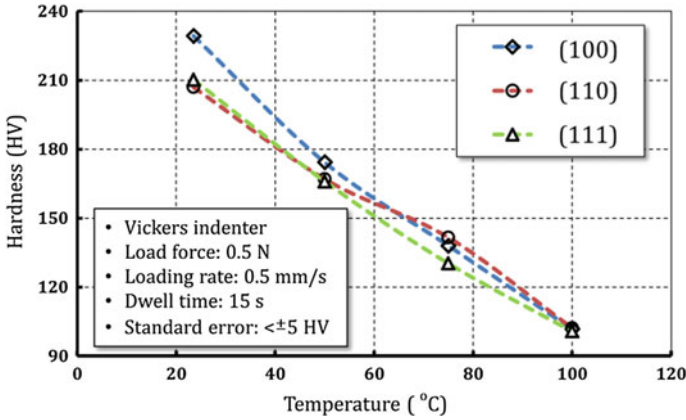


**Fig. 13** Decrease in hardness of CaF<sub>2</sub> single crystals with increase in temperature [24]

resistance on the (110) plane-oriented CaF<sub>2</sub> sample that has the highest tendency for brittle failure by cleaving shown by Azami et al. [20]. Additionally, based on Eq. 1, it can be understood that a trend of increasing fracture toughness is a resultant cause of the rise in material temperature and therefore enables the material to undergo enhanced plastic deformation at higher yield stresses.

### 3.2 Heat-Assisted Machining Simulations

More than one slip system can be activated at higher temperatures when conducting compression tests along different crystallographic directions of CaF<sub>2</sub> single crystals [36]. Conventional theories on the motion of dislocations are necessary to understand the influence of slip systems and plastic deformation. The motion of a dislocation occurs through the shifts of the adjacent atoms but encounters obstacles like the short-ranged Peirels–Nabarro energy barrier. However, the energy required for the displacement of atoms can be easily overcome with a thermally assisted applied force and promotes plastic deformation [37]. Therefore, the energy for slip to occur would be reduced to precede the occurrence of brittle fracture. In compression tests at room temperature, the {100} plane of CaF<sub>2</sub> is the only slip plane [36]. Subsequently when heated to temperatures between 90 and 400 °C, the {111} slip plane was activated and a third {110} slip plane was activated at temperatures above 400 °C [36].

Theoretical simulations for orthogonal microcutting can be developed for establishment of the theoretical foundation for the material removal process at room and elevated temperatures associated with the experimentally proven number of slip planes that were thermally activated. Wang et al. [32] developed a CPFEM model to theoretically describe the effect of the activated slip systems during orthogonal cutting. In their work, three different models were created to simulate the cutting of

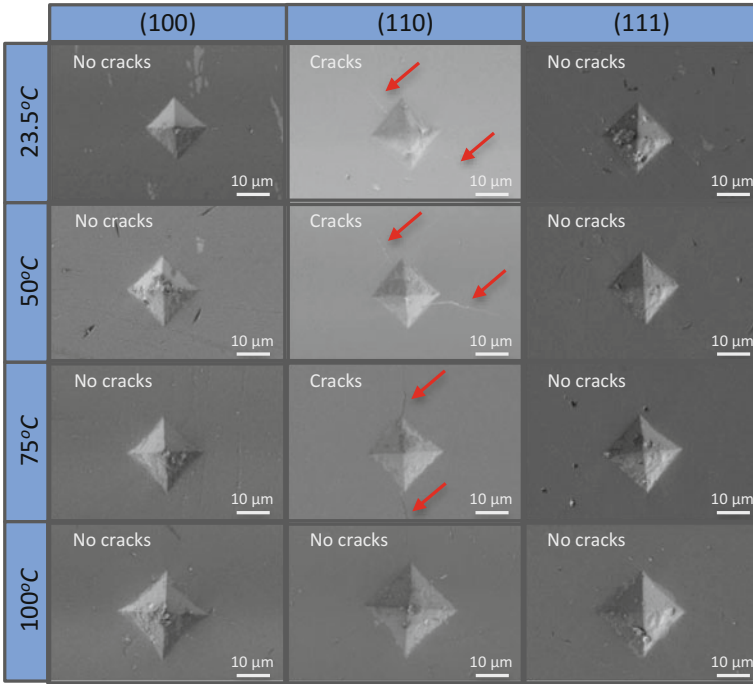


**Fig. 14** SEM images of microhardness indentations on the (100), (110), and (111) plane orientations of CaF<sub>2</sub> single crystals over a range of temperatures [24]

CaF<sub>2</sub> single crystals at the room temperature, 200 °C, and 400 °C. The cumulative shear strain plots of each model simulated for the different number of activated systems in Fig. 15 show the increase in plasticity due to the dislocation activities ahead of the cutting tool. Defects in the material act as nuclei for cleavage fracture, and a larger stress field at the cutting edge could allow a larger density of defects to initiate cleavage fracture [15]. Under room temperature conditions, the size effect is commonly controlled by the undeformed chip thickness where a small undeformed chip thickness would result in a smaller critical stress field. At elevated temperatures, the critical stress field size is simulated to decrease, thus reducing the interaction with subsurface defects.

CPFEM is also capable of verifying the trend observed in the experimental results from Sect. 3.1, where a reduction in anisotropic characteristics is realized for elevated temperatures. Two sides of the model can be shown to review the influence of the material anisotropy that would result in the asymmetric deformation. The asymmetric ductile–brittle transition (aDBT) is an important aspect of the ductile–brittle transition study in view of the lateral forces induced during different types of crack formations. An asymmetric orthogonal groove results in unbalanced lateral force fluctuations with a feature of lamellar cracks on one side of the groove as shown in Fig. 16 [21]. Balanced forces can be observed with more symmetrical types of

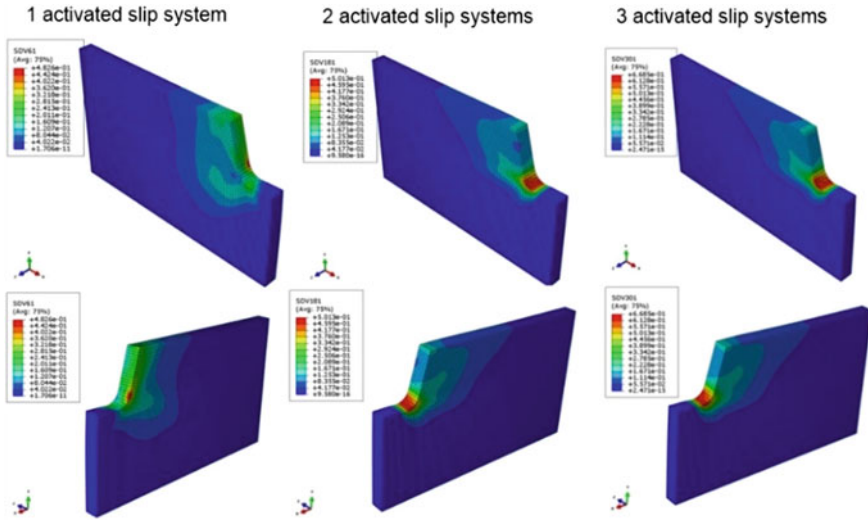


**Fig. 15** CPFEM simulations of cumulative shear strain on all slip systems during ductile-regime cutting for one, two, and three activated systems at 25, 200, and 400 °C, respectively [32] (recreated with permission from SAGE Publications © 2016)

grooving that feature different types of crack morphology due to the relative cutting direction with respect to the cleavage plane.

The simulated result for one activated slip system in Fig. 15 shows the differences in the cumulative shear strains on each side of the model attributed to the asymmetric feature. At higher temperatures, the asymmetric feature loses prominence when more slip systems are activated, and the anisotropic effect is severely reduced. Simulated results of the 200 and 400 °C case with two and three activated slip systems show similarities in the cumulative shear strain plots on both sides of the model, signifying the transition to an isotropic material at higher temperatures.

As expected, the simulated lateral forces in Fig. 17a are further reduced and rendered negligible at elevated temperatures where two and three sets of slip system are active. Simulated cutting and thrust forces also show a reduction of approximately 50% in Fig. 17b when heated from room temperature with one activated slip system to 200 and 400 °C with more slip systems thermally activated. The thermally activated slip systems allow the movement of dislocations and thus increasing the plasticity of the material being removed.

Therefore, it can be understood from theoretical simulations that thermally assisted machining has multiple benefits to enhance the machinability of the brittle material. The benefits observed from experimental and theoretical results are as summarized below:

- Linear reduction in hardness,
- Activation of secondary and tertiary slip systems,
- Reducing anisotropic properties of single crystals.



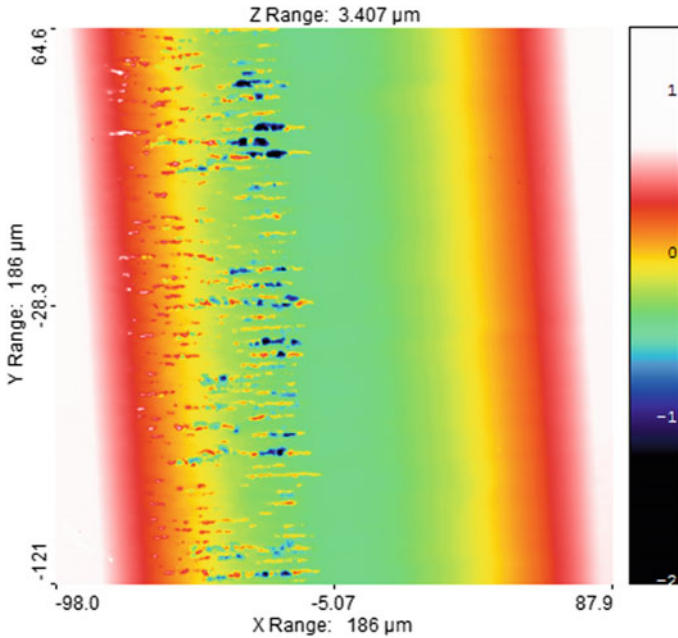


**Fig. 16** WLI image of asymmetric ductile–brittle transition along a groove [21] (recreated with permission from SAGE Publications © 2016)

## 4 Thermally Assisted Machining Technology

### 4.1 Current State of Technology

Many strategies have been investigated to improve the machinability of difficult-to-machine materials. Thermally assisted machining is one of the advancing methods used in the aerospace and automotive industry for difficult-to-machine superalloy materials. Although there are many types of heating methods, the induction heating, laser heating, and plasma arc heating are the most promising methods to be adopted in conventional machining. Each method generally aims to reduce the cutting forces during machining and improve the material removal rate efficiencies while prolonging cutting tool life. The detailed comparison between each method is described in Table 2. The effectiveness of thermally assisted machining depends on the conventional cutting parameters such as cutting speed and heating parameters such as the distance between the localized heating zone and the tool cutting edge and the amount of supplied heat energy. The common benefits of the thermally assisted machining techniques are summarized below [38–44]:

- Improved surface finish,
- Improved cutting tool life,

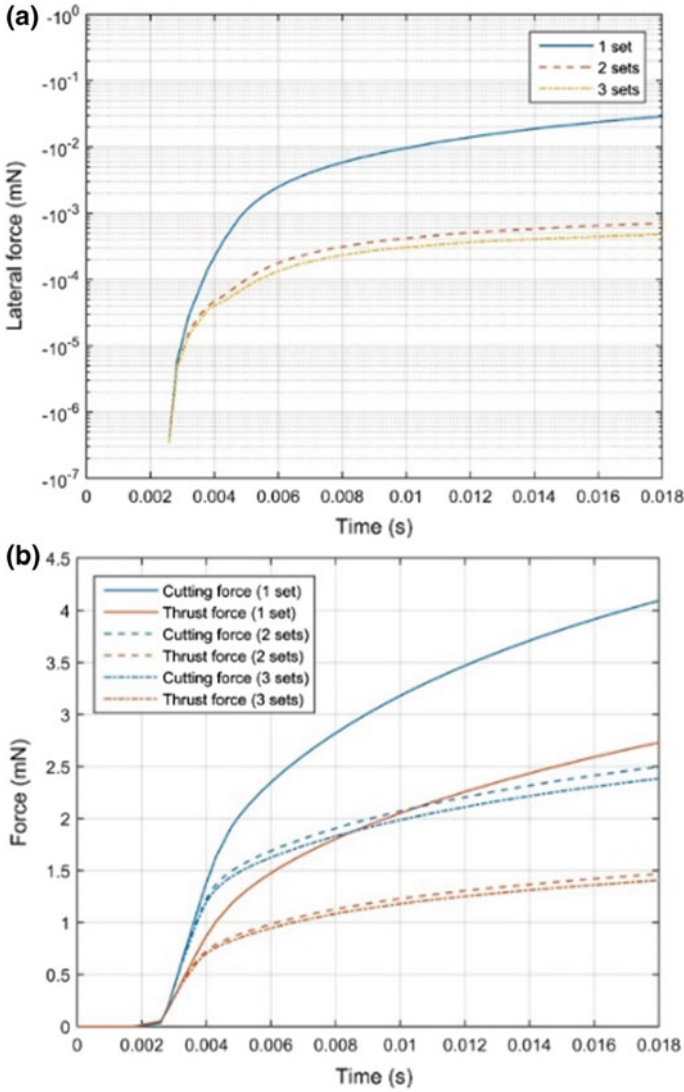


**Fig. 17** Simulation forces during orthogonal cutting of one, two, and three activated slip system sets: **a** lateral force; **b** cutting and thrust forces [32] (recreated with permission from SAGE Publications © 2016)

- Increased material removal rates,
- Reduced machining forces,
- Reduced residual stresses,
- Reduced chattering and machining vibrations.

**Table 2** Thermally assisted machining methods [45–47]

	Induction heating	Laser heating	Plasma heating
Heat source	Electric current	Laser	Plasma arc
Source mobility	Rigid	Flexible	Flexible
Temperature range	Low	High	High
Advantages	<ul style="list-style-type: none"> <li>• Easy to regulate</li> <li>• Stable temperatures</li> </ul>	<ul style="list-style-type: none"> <li>• Stable and flexible heat distribution</li> </ul>	<ul style="list-style-type: none"> <li>• No metallurgical damage to workpiece</li> <li>• Economical</li> </ul>
Disadvantages	<ul style="list-style-type: none"> <li>• Heat induction in a line (delocalized)</li> </ul>	<ul style="list-style-type: none"> <li>• Costly</li> <li>• Material-dependent absorption rates</li> </ul>	<ul style="list-style-type: none"> <li>• Inaccurate control of localized heating temperature</li> </ul>

## 4.2 Laser-Assisted Machining

Over the last few decades, much work has been done on thermally assisted machining that has been dedicated to conventional macroscale machining processes such as turning, grinding, and milling. But with the advancement in optical technology, thermal assistance has thus shifted its focus toward laser-assisted machining (LAM). LAM was first introduced by Bass et al. [48] in 1978, inspired by the adoption of gas torch and induction heating for heat-assisted machining. A common heat-assisted setup as illustrated in Fig. 18 involves installing a conventional setup with an external heat source to produce a localized heat spot to soften the mechanically hard workpiece ahead of the cutting tool [39, 42]. Noncontact thermal sensing equipment, such as an infrared camera, is often used to measure the degree of heating of the workpiece. When the high-power laser heats the workpiece, the material yield strength and hardness values decrease below the fracture strength, thus allowing the material to be removed in the ductile-regime. LAM commonly employs the use of the CO<sub>2</sub> laser and Nd:YAG laser, but the latter is a better candidate due to its higher absorption rates of laser energy [49].

From conventional machining theories, a higher feed rate increases the volume of material removed per revolution, which is proportional to the increase in cutting forces. However, the opposite is observed when machining with LAM. Few differences in the cutting forces at low feeds were reported when machining Ti-6Cr-5Mo-5V-4Al titanium alloy with and without LAM, but a 12% reduction in cutting forces with LAM was measured upon increasing the feed rate [44]. Therefore, it is obvious that LAM allows more productive machining efficiencies in terms of material removal rates and tool life when handling difficult-to-machine materials.

Much work on the adoption of LAM has been focused on improving the machinability of difficult-to-machine materials in the macroscale. Micro-laser-assisted machining ( $\mu$ -LAM) techniques are the latest advancement of heat addition methods by laser irradiation. Unlike conventional methodologies of heating a spot of the workpiece a distance ahead of the cutting tool,  $\mu$ -LAM process beams an IR diode

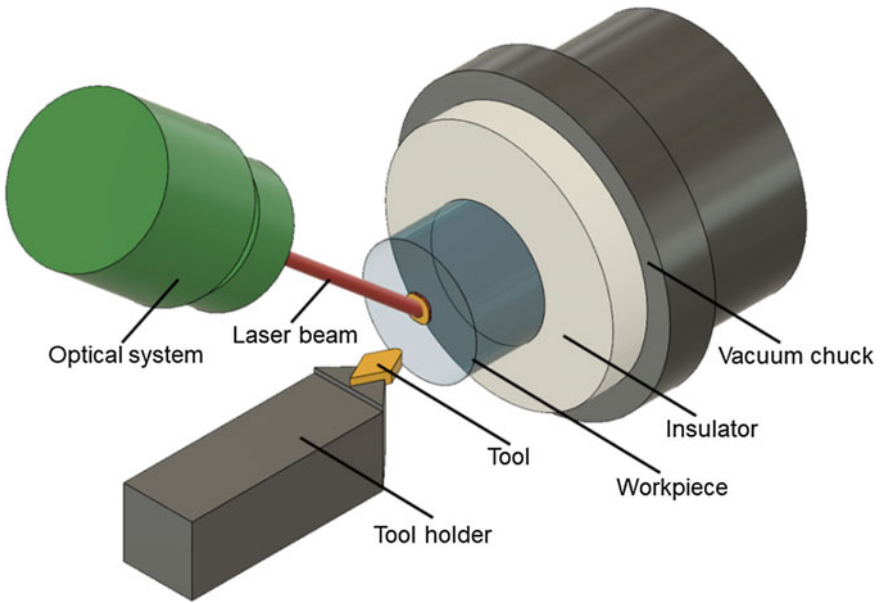


**Fig. 18** Laser-assisted machining turning schematic

laser ( $\lambda = 1070$  nm) through the diamond cutting tool to the tool–workpiece interface as shown in Fig. 19 [50]. The thermal softening efficiency of this method during an actual machining process can be observed through basic tribology tests. Shayan et al. [51] equipped a universal micro-tribometer (UMT) with the  $\mu$ -LAM technique and conducted scratch tests on 4H SiC with a diamond stylus under varying speeds but a constant applied load. They reported a minor increase in groove depth by 5 nm when testing at higher cutting speeds. However, at extremely low cutting speeds, the average groove depth increased significantly from 54 to 90 nm. The thermal softening effect can therefore be concluded to be less prominent at higher cutting speeds when using the  $\mu$ -LAM technique.

Optimization of the heating parameters is essential to achieve the desired surface quality. Surprisingly, there exists a critical value of laser power for ductile-regime machining, and an excess laser power applied could result in poorer surface finishing. Mohammadi et al. [52] employed the  $\mu$ -LAM on an SPDT process of silicon single crystal and found an increase in Ra value by a factor of 1.6 when the laser power was increased from 20 to 30 W. It was also added that the advantages of this technique were the capability of conducting a thermally assisted machining process accompanied with cutting fluids. This is one of the major advantages of the fast contactless heating method as shown in Fig. 19. With the  $\mu$ -LAM technique, they were able to conduct ductile-mode machining at a higher undeformed chip thickness value to achieve a mirror-like surface finishing on the silicon single crystal as shown in Fig. 20.

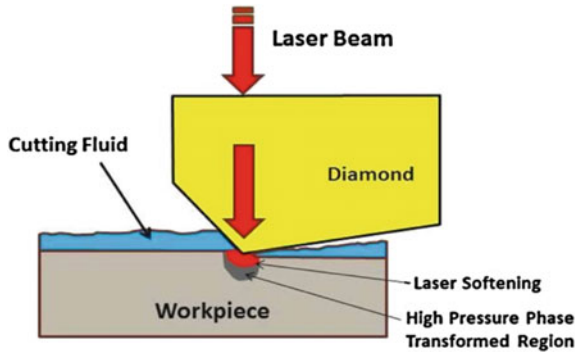


**Fig. 19** Schematic of the  $\mu$ -LAM process with cutting fluids [52] (recreated with permission from Elsevier © 2015)

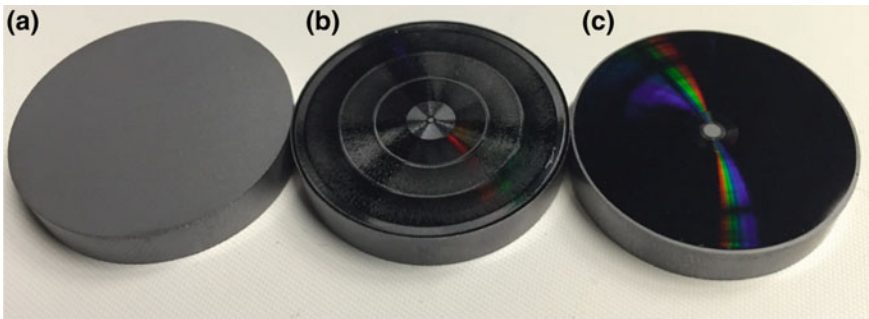


**Fig. 20** **a** As received; **b** conventional micromachining; **c** with  $\mu$ -LAM technique [52] (recreated with permission from Elsevier © 2015)

### 4.3 Alternate Heating Methods

While most thermally assisted machining methods use a localized heat source shown by the schematic in Fig. 18, it is interesting to note that most static experimental tests such as the heated nanoindentation test can be conducted with a globalized heat source. The global heating method may be defined by applying heat to the sample and to achieve an evenly heated sample in Fig. 21.

In some cases, heat is also applied to the machine tool to reduce abrupt fluctuations in heat transfer. Korte et al. [53] developed a customized hot nanoindentation setup that operates in vacuum to study the thermal stability and instrument noises caused by the impurities of inert gases during high-temperature testing. Resistive heaters were applied to both the indenter and the sample. A drastic temperature difference between a room temperature indenter and heated sample may cause unwanted undesired expansion and contraction at the interface, causing dimensional changes that disrupt the experiment [53].

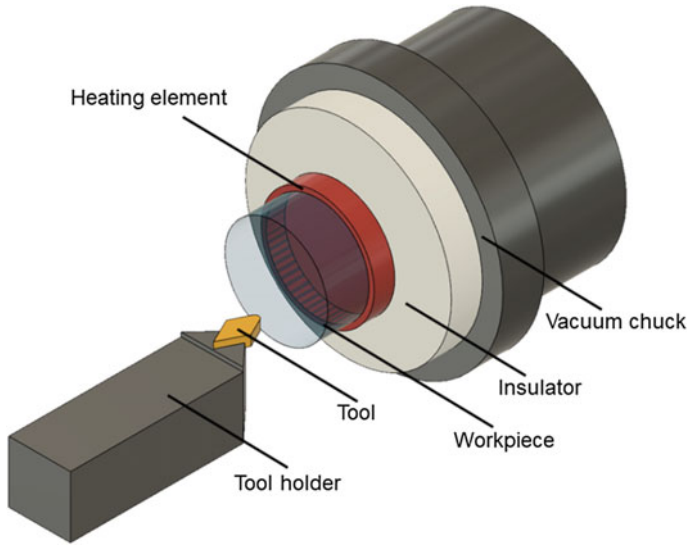


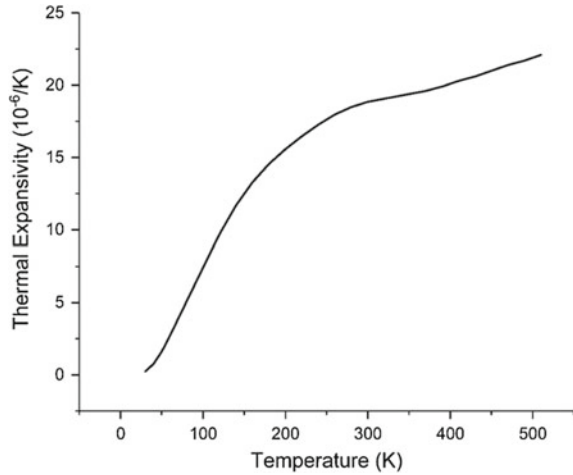
**Fig. 21** Orthogonal cutting schematic with **a** localized heating and **b** global heating methods

#### **4.4 Challenges in Hot Machining**

Till date, there have not been any official publications on the use of the  $\mu$ -LAM technique or any contactless heating method integrated into the machining process of  $\text{CaF}_2$ . Different types of heat sources are still being explored to improve the machinability of  $\text{CaF}_2$ . In general, several complications have arisen in the use of thermally assisted machining. Experimentation and industrial use of hot machining in ambient environments potentially promote the formation of an oxide layer on the pre-machined or machined surface, which could substantially affect the material removal mechanisms in the submicron range. Oxidation proof coatings on the sample surface or experimentation in an inert environment help with the oxidation problem. However, different materials oxidize at different temperatures and environments. For example, it is recommended to coat copper with a thin layer of platinum to prevent oxidation during nanoindentation tests in the lower range of elevated temperatures ( $>200^\circ\text{C}$ ) [54]. Oxygen is known to penetrate  $\text{CaF}_2$  at elevated temperatures and begin precipitation when cooled below  $725^\circ\text{C}$  [55].

High-accuracy temperature control equipment is extremely important in this aspect when taking material thermal expansion into consideration. This is particularly crucial when machining with submicron undeformed chip thickness values. As seen in Fig. 22, a slight deviation in temperature would cause a material expansion or contraction at a magnitude similar to the desired undeformed chip thickness. A basic temperature control setup would commonly include temperature controllers, a heat source, and temperature measurement devices.

**Fig. 22** Thermal expansion of  $\text{CaF}_2$  [56, 57]



In summary, thermally assisted machining has been proven to improve the machining process of difficult-to-machine and brittle materials in various ways. A detailed description of a systematic experimental process had been discussed with the ductile–brittle transition explained using the well-established slip theory. However, the application of such technology on  $\text{CaF}_2$  single crystals has only been limited to the preliminary studies using indentation tests at elevated temperatures. The challenges in achieving thermally assisted ductile-mode machining of  $\text{CaF}_2$  have been briefly explained to serve as a foundation for considerations in the future works of this field.

**Acknowledgements** The authors are grateful for the financial support from National University of Singapore Start-up Grant (Grant No.: R-265-000-564-133) and Singapore Ministry of Education Academic Research Fund Tier 1 (Grant No.: R-265-000-593-114).

## References

1. Dao GT, Borodovsky YA (2001) 157-nm lithography for 100-nm generation and beyond: progress and status. In: Proceeding of SPIE 4186, 20th annual BACUS symposium on photomask technology
2. Rothschild M, Bloomstein TM, Fedynyshyn TH, Kunz RR, Liberman V, Switkes M, Efremov NN, Palmacci ST, Sedlacek JHC, Hardy DE, Grenville A (2003) Optical lithography. *Lincoln Lab J* 14:221–236
3. Hahn D (2014) Calcium fluoride and barium fluoride crystals in optics: multispectral optical materials for a wide spectrum of applications. *Opt Photonik* 9:45–48
4. Nachimuthu S, Aoshima M, Shimizu S, Sumiya K, Ishibashi H (2007) Improvement in optical properties of  $\text{CaF}_2$  single crystals used for nanolithography
5. Elswie HI, Lazarevi ZŽ, Radojevi V, Gili M, Rabasovi M, Ševi D, Rom NŽ (2016) The Bridgman method growth and spectroscopic characterization of calcium fluoride single crystals. *Sci Sinter* 48:333–341. <https://doi.org/10.2298/SOS1603333E>

6. Ko JM, Tozawa S, Yoshikawa A, Inaba K, Shishido T (2001) Czochralski growth of UV-grade  $\text{CaF}_2$  single crystals using  $\text{ZnF}_2$  additive as scavenger. *J Cryst Growth* 222:243–248
7. Mouchovski JT, Penev VT, Kuneva RB (1996) Control of the growth optimum in producing high-quality  $\text{CaF}_2$  crystals by an improved Bridgman-Stockbarger technique. *Cryst Res Technol* 31:727–737
8. Lambropoulos JC, Xu S, Fang T (1997) Loose abrasive lapping hardness of optical glasses and its interpretation. *Appl Opt* 36:1501–1516
9. Wang Z, Wu Y, Dai Y, Li S (2008) Subsurface damage distribution in the lapping process. *Appl Opt* 47:1417–1426
10. Yan J, Tamaki J, Syoji K, Kuriyagawa T (2004) Single-point diamond turning of  $\text{CaF}_2$  for nanometric surface. *Int J Adv Manuf Technol* 24:640–646. <https://doi.org/10.1007/s00170-003-1747-2>
11. Shibata T, Fujii S, Makino E, Ikeda M (1996) Ductile-regime turning mechanism of single-crystal silicon. *Precis Eng* 18:129–137
12. Puttick KE, Rudman MR, Smith KJ, Franks A, Lindsey K (1989) Single-point diamond machining of glasses. *Proc R Soc London A Math Phys Sci* 426:19–30
13. Blackley WS, Scattergood RO (1991) Ductile-regime machining model for diamond turning of brittle materials. *Precis Eng* 13:95–103. [https://doi.org/10.1016/0141-6359\(91\)90500-I](https://doi.org/10.1016/0141-6359(91)90500-I)
14. O'Neill JB, Redfern BAW, Brookes CA (1973) Anisotropy in the hardness and friction of calcium fluoride crystals. *J Mater Sci* 8:47–58. <https://doi.org/10.1007/BF00755582>
15. Nakasuji T, Kodera S, Hara S, Ikawa N (1990) Diamond turning of brittle materials for optical components. *CIRP Ann Manuf Technol* 39:89–92
16. Shimada S, Ikawa N, Toyoshiro I, Nobuhiro T, Hitoshi O, Toshio S (1995) Brittle-ductile transition phenomena in microindentation and micromachining. *Ann CIRP* 44:523–526
17. Mizumoto Y, Kakinuma Y (2018) Revisit of the anisotropic deformation behavior of single-crystal  $\text{CaF}_2$  in orthogonal cutting. *Precis Eng* 53:9–16. <https://doi.org/10.1016/j.precisioneng.2018.01.011>
18. Lodes MA, Hartmaier A, Göken M, Durst K (2011) Influence of dislocation density on the pop-in behavior and indentation size effect in  $\text{CaF}_2$  single crystals: experiments and molecular dynamics simulations. *Acta Mater* 59:4264–4273. <https://doi.org/10.1016/j.actamat.2011.03.050>
19. Mizumoto Y, Aoyama T, Kakinuma Y (2011) Basic study on ultraprecision machining of single-crystal calcium fluoride. *Procedia Eng* 19:264–269. <https://doi.org/10.1016/j.proeng.2011.11.110>
20. Azami S, Kudo H, Mizumoto Y, Tanabe T, Yan J, Kakinuma Y (2015) Experimental study of crystal anisotropy based on ultra-precision cylindrical turning of single-crystal calcium fluoride. *Precis Eng* 40:172–181. <https://doi.org/10.1016/j.precisioneng.2014.11.007>
21. Wang H, Riemer O, Rickens K, Brinksmeier E (2016) On the mechanism of asymmetric ductile-brittle transition in microcutting of (111)  $\text{CaF}_2$  single crystals. *Scr Mater* 114:21–26. <https://doi.org/10.1016/j.scriptamat.2015.11.030>
22. Chen X, Xu J, Fang H, Tian R (2017) Influence of cutting parameters on the ductile-brittle transition of single-crystal calcium fluoride during ultra-precision cutting. *Int J Adv Manuf Technol* 89:219–225. <https://doi.org/10.1007/s00170-016-9063-9>
23. Marsh ER, John BP, Couey JA, Wang J, Grejda RD, Vallance RR (2005) Predicting surface figure in diamond turned calcium fluoride using in-process force measurement. *J Vac Sci Technol B Microelectron Nanom Struct* 23:84. <https://doi.org/10.1116/1.1839897>
24. Chaudhari A, Lee YJ, Wang H, Senthil Kumar A (2017) Thermal effect on brittle-ductile transition in  $\text{CaF}_2$  single crystals. In: Proceedings of the 17th international conference of the European Society for precision engineering and nanotechnology, EUSPEN 2017
25. Cook RF, Pharr GM (1990) Direct observation and analysis of indentation cracking in glasses and ceramics. *J Am Ceram Soc* 73:787–817. <https://doi.org/10.1111/j.1151-2916.1990.tb05119.x>
26. Fang FZ, Chen LJ (2000) Ultra-precision cutting for ZKN7 glass. *CIRP Ann Manuf Technol* 49:17–20. [https://doi.org/10.1016/S0007-8506\(07\)62887-X](https://doi.org/10.1016/S0007-8506(07)62887-X)



27. Yan J, Asami T, Harada H, Kuriyagawa T (2009) Fundamental investigation of subsurface damage in single crystalline silicon caused by diamond machining. *Precis Eng* 33:378–386. <https://doi.org/10.1016/j.precisioneng.2008.10.008>
28. Kawasegi N, Niwata T, Morita N, Nishimura K, Sasaoka H (2014) Improving machining performance of single-crystal diamond tools irradiated by a focused ion beam. *Precis Eng* 38:174–182. <https://doi.org/10.1016/j.precisioneng.2013.09.001>
29. O'Connor BP, Marsh ER, Couey JA (2005) On the effect of crystallographic orientation on ductile material removal in silicon. *Precis Eng* 29:124–132. <https://doi.org/10.1016/j.precisioneng.2004.05.004>
30. Blake PN, Scattergood RO (1990) Ductile-regime machining of germanium and silicon. *J Am Ceram Soc* 73:949–957. <https://doi.org/10.1111/j.1151-2916.1990.tb05142.x>
31. Yan J, Syoji K, Tamaki J (2004) Crystallographic effects in micro/nanomachining of single-crystal calcium fluoride. *J Vac Sci Technol B Microelectron Nanom Struct* 22:46. <https://doi.org/10.1116/1.1633770>
32. Wang H, Senthil Kumar A, Riemer O (2016) On the theoretical foundation for the microcutting of calcium fluoride single crystals at elevated temperatures. *Proc Inst Mech Eng Part B J Eng Manuf* 1–7. <https://doi.org/10.1177/0954405416666907>
33. Yan J, Asami T, Harada H, Kuriyagawa T (2012) Crystallographic effect on subsurface damage formation in silicon microcutting. *CIRP Ann Manuf Technol* 61:131–134. <https://doi.org/10.1016/j.cirp.2012.03.070>
34. Xiao G, To S, Zhang G (2015) Molecular dynamics modelling of brittle-ductile cutting mode transition: case study on silicon carbide. *Int J Mach Tools Manuf* 88:214–222. <https://doi.org/10.1016/j.ijmactools.2014.10.007>
35. Deadmore DL, Sliney HE (1987) Hardness of CaF<sub>2</sub> and BaF<sub>2</sub> solid lubricants at 25 to 670 °C (NASA Technical Memorandum 88979)
36. Muñoz A, Domínguez-Rodríguez A, Castaing J (1994) Slip Systems and plastic anisotropy in CaF<sub>2</sub>. *J Mater Sci* 29:6207–6211. <https://doi.org/10.1007/BF00354561>
37. Conrad H (1964) Thermally activated deformation of metals. *J Met* 16:582–588. <https://doi.org/10.1007/BF03378292>
38. López de Lacalle LN, Sánchez JA, Lamikiz A, Celaya A (2004) Plasma assisted milling of heat-resistant superalloys. *J Manuf Sci Eng* 126:274. <https://doi.org/10.1115/1.1644548>
39. Kumar M, Melkote S, Lahoti G (2011) Laser-assisted microgrinding of ceramics. *CIRP Ann Manuf Technol* 60:367–370. <https://doi.org/10.1016/j.cirp.2011.03.121>
40. Ding H, Shen N, Shin YC (2012) Thermal and mechanical modeling analysis of laser-assisted micro-milling of difficult-to-machine alloys. *J Mater Process Technol* 212:601–613. <https://doi.org/10.1016/j.jmatprotec.2011.07.016>
41. Ding H, Shin YC (2010) Laser-assisted machining of hardened steel parts with surface integrity analysis. *Int J Mach Tools Manuf* 50:106–114. <https://doi.org/10.1016/j.ijmactools.2009.09.001>
42. Tian Y, Wu B, Anderson M, Shin YC (2008) Laser-assisted milling of silicon nitride ceramics and inconel 718. *J Manuf Sci Eng* 130:031013. <https://doi.org/10.1115/1.2927447>
43. Lei S, Shin YC, Incropera FP (2001) Experimental investigation of thermo-mechanical characteristics in laser-assisted machining of silicon nitride ceramics. *J Manuf Sci Eng* 123:639. <https://doi.org/10.1115/1.1380382>
44. Rahman Rashid RA, Sun S, Wang G, Dargusch MS (2012) An investigation of cutting forces and cutting temperatures during laser-assisted machining of the Ti-6Cr-5Mo-5 V-4Al beta titanium alloy. *Int J Mach Tools Manuf* 63:58–69. <https://doi.org/10.1016/j.ijmactools.2012.06.004>
45. Madhavulu G, Ahmed B (1994) Hot machining process for improved metal removal rates in turning operations. *J Mater Process Tech* 44:199–206. [https://doi.org/10.1016/0924-0136\(94\)90432-4](https://doi.org/10.1016/0924-0136(94)90432-4)
46. Jeon Y, Lee CM (2012) Current research trend on laser assisted machining. *Int J Precis Eng Manuf* 13:311–317. <https://doi.org/10.1007/s12541-012-0040-4>

47. Shams OA, Pramanik A, Chandratilleke TT (2017) Thermal-assisted machining of titanium alloys. In: Gupta K (ed) *Advanced manufacturing technologies*. Springer International Publishing, Berlin, pp 49–76
48. Bass M, Beck D, Copley SM (1979) Laser assisted machining. In: *Proceeding of SPIE 0164, 4th European electro-optics conference*, pp 233–240
49. Venkatesan K, Ramanujam R, Kuppan P (2014) Laser assisted machining of difficult to cut materials: Research opportunities and future directions - A comprehensive review. *Procedia Eng* 97:1626–1636. <https://doi.org/10.1016/j.proeng.2014.12.313>
50. Ravindra D, Ghantasala MK, Patten J (2012) Ductile mode material removal and high-pressure phase transformation in silicon during micro-laser assisted machining. *Precis Eng* 36:364–367
51. Shayan AR, Poyraz HB, Ravindra D, Patten JA (2009) Pressure and temperature effects in micro-laser assisted machining ( $\mu$ -LAM) of silicon carbide. *Trans North Am Manuf Res Inst SME* 37:75–80
52. Mohammadi H, Ravindra D, Kode SK, Patten JA (2015) Experimental work on micro laser-assisted diamond turning of silicon (111). *J Manuf Process* 19:125–128. <https://doi.org/10.1016/j.jmapro.2015.06.007>
53. Korte S, Stearn RJ, Wheeler JM, Clegg WJ (2011) High temperature microcompression and nanoindentation in vacuum High temperature microcompression and nanoindentation in vacuum. *J Mater Res* 27:167–176. <https://doi.org/10.1557/jmr.2011.268>
54. Duan ZC, Hodge AM (2009) High-temperature nanoindentation: new developments and ongoing challenges. *J Miner Met Mater Soc* 62:32–36
55. Phillips WL, Hanlon JE (1963) Oxygen penetration into single crystals of calcium fluoride. *J Am Ceram Soc* 46:447–449
56. Batchelder DN, Simmons RO (1964) Lattice constants and thermal expansivities of silicon and of calcium fluoride between 6° and 322°K. *J Chem Phys* 41:2324–2329. <https://doi.org/10.1063/1.1726266>
57. Ballard SS, Brown SE, Browder JS (1978) Measurements of the thermal expansion of six optical materials, from room temperature to 250 °C. *Appl Opt* 17:1152. <https://doi.org/10.1364/AO.17.001152>
58. Beake BD, Smith JF (2002) High-temperature nanoindentation testing of fused silica and other materials. *Philos Mag A Phys Condens Matter, Struct Defects Mech Prop* 82:2179–2186. <https://doi.org/10.1080/01418610208235727>
59. Michel MD, Serbena FC, Lepienski CM (2006) Effect of temperature on hardness and indentation cracking of fused silica. *J Non Cryst Solids* 352:3550–3555. <https://doi.org/10.1016/j.jnoncrysol.2006.02.113>